



HAL
open science

Transient hillslope erosion in slow evolution landscapes

Vincent Godard, Salgado A., Siame L., Jules Fleury, Team Aster

► **To cite this version:**

Vincent Godard, Salgado A., Siame L., Jules Fleury, Team Aster. Transient hillslope erosion in slow evolution landscapes. *Earth Surface Processes and Landforms*, 2021, 46 (12), pp.2485-2500. 10.1002/esp.5190 . hal-03346897v1

HAL Id: hal-03346897

<https://amu.hal.science/hal-03346897v1>

Submitted on 16 Sep 2021 (v1), last revised 16 Nov 2021 (v2)

HAL is a multi-disciplinary open access archive for the deposit and dissemination of scientific research documents, whether they are published or not. The documents may come from teaching and research institutions in France or abroad, or from public or private research centers.

L'archive ouverte pluridisciplinaire **HAL**, est destinée au dépôt et à la diffusion de documents scientifiques de niveau recherche, publiés ou non, émanant des établissements d'enseignement et de recherche français ou étrangers, des laboratoires publics ou privés.

1 Transient hillslope erosion in slow evolution landscapes

2 Godard V.^{1,2,a}, Salgado A.³, Siame L.¹, Fleury J.¹ and ASTER Team^{1,*}

3 September 16, 2021

4 ¹Aix-Marseille Univ, CNRS, IRD, INRAE, Coll France, CEREGE, 13545, Aix-en-Provence,
5 France

6 ²Institut Universitaire de France (IUF), 75231, Paris, France

7 ³Department of Geography, Minas Gerais Federal University, CEP 31270-901 Belo Hori-
8 zonte MG, Brazil

9
10 ^a Corresponding author : godard@cerege.fr

11 ^{*} Georges Aumaître, Didier L. Bourlès, Karim Keddadouche

12 Published in V., Godard, A., Salgado, L., Siame, J., Fleury & ASTER Team (2021)
13 Transient hillslope erosion in slow evolution landscapes. *Earth Surface Processes and Land-*
14 *forms*, 46(12), 2485-2500 ([10.1002/esp.5190](https://doi.org/10.1002/esp.5190))

15 Abstract

16 Transient evolution and adjustment to changing tectonic and climatic boundary
17 conditions is an essential attribute of landscapes and characterizing transient behav-
18 ior is a key to understand their dynamics and history. Developing new approaches to
19 detect such transience has been explored by various methods, in particular to iden-
20 tify landscape response to Late Cenozoic and Quaternary climatic changes. Such
21 studies have often focused on regions of high relief and/or active tectonic activity
22 where interferences between tectonic and climatic signals might complicate the inter-
23 pretation of the observations. We investigated the case of the hillslopes of the Serra
24 do Cipó quartzitic range in SE Brazil in order to detect and quantify transience in a
25 tectonically-quiet landscape over 100 ka timescales. We determined hilltop cur-
26 vature from a high resolution Digital Surface Model derived from Pléiades imagery
27 and measured cosmogenic nuclide concentrations (¹⁰Be and ²⁶Al) at these hilltop

28 sites. We compare both observations with predictions of hillslope diffusion theory,
29 and observe a distinctive signature of an acceleration of denudation. We performed
30 a joint inversion of topographic and isotopic data to retrieve an evolution of hillslope
31 sediment transport coefficient through time. The timing of the increase in denuda-
32 tion cannot be unequivocally associated with a single climatic event but is consistent
33 with climatically-modulated important fluctuations in precipitation and erosion in
34 this area during Middle and Late Pleistocene.

35 **1 Introduction**

36 The Earth surface acts as a major interface between internal and external geodynamics,
37 and is the focus of many investigations concerning the complex network of processes con-
38 necting surface processes, tectonics and climate [e.g. [Champagnac et al., 2012](#)]. Notably,
39 a key element of this system is the degree of coupling between climatic variations and
40 denudation, which is fundamental to assess the strength of many postulated feedbacks
41 between the atmosphere and the dynamics of weathering, sediment production and trans-
42 port across continental surfaces. Over short time scales, many observations support the
43 key role of temperature and precipitation conditions in directly controlling the modes and
44 rates of weathering of materials transiting through regolith profiles, as well as their ex-
45 port across and beyond hillslopes domain [e.g. [Gaillardet et al., 1999](#); [Hales and Roering,](#)
46 [2005](#); [Gabet et al., 2008](#); [West et al., 2014](#)]. However, when integrating these processes
47 over larger spatial and temporal frames, highly contrasting propositions have been made
48 concerning the actual relationship between surface processes acting on continental relief
49 and climatic evolution, over the Late Cenozoic. In particular, an important question still
50 actively debated concerns whether or not Late Cenozoic cooling was associated with a
51 global increase in denudation rates [e.g. [Herman and Champagnac, 2016](#); [Willenbring and](#)
52 [Jerolmack, 2016](#); [Norton and Schlunegger, 2017](#)], suggesting that additional investigations

53 using novel methodologies are needed to better resolve denudation variations and transient
54 landscape dynamics through time.

55 Regions of high relief or tectonic activity have often been the primary target of studies
56 focusing on climate-denudation links, using the sedimentary archives resulting from the
57 erosional fluxes in such areas [e.g. [Charreau et al., 2011](#); [Lenard et al., 2020](#)]. However,
58 important limitations can be encountered in this type of settings, such as high denuda-
59 tion rates reaching the analytical limits of many measurement methods, or gaps in the
60 sedimentary records and stochastic events introducing a high degree of variability in the
61 denudation signal. Additionally, temporal and spatial variations of the tectonic boundary
62 condition can be difficult to deconvolve from the record and complicate interpretations in
63 terms of climatic influence on surface processes.

64 Conversely, areas of low tectonic activity may provide propitious conditions allowing the
65 investigation of the coupling between climate variations and surface processes. However,
66 long-duration continental sedimentary archives, spanning several 100s ka or Ma, are of-
67 ten scarce in such settings so alternative approaches are required to develop longer-term
68 records of landscape transience and assess its link with climatic evolution [[Struck et al.,](#)
69 [2018](#)]. When measuring active denudation, as opposed to paleo-denudation records in sedi-
70 mentary archives, slow landscape evolution also implies long integration timescales for most
71 geochronological techniques, such as cosmogenic nuclides, which might provide insights on
72 the dynamics of surface processes over 100s ka to several Ma. This time frame is at least
73 one order of magnitude longer to that usually encountered in active orogenic settings.

74 Terrestrial Cosmogenic Nuclides (TCN) are one of the most widely used tools to constrain
75 the distribution of denudation rates at the Earth surface over 1 ka-1 Ma timescales [[von](#)
76 [Blanckenburg, 2005](#)]. Attempts to recover information on past denudation conditions have
77 mostly focused on TCN time-series in the sedimentary record. However, combinations of
78 several cosmogenic nuclides, with different decay constants, offer the possibility to identify

79 transient dynamics resulting from changes in denudation rates through time [Mudd, 2016].
80 For example, the promising ^{10}Be - ^{14}C pair has been used to decipher complex dynamics
81 of surface processes over Holocene time scales [Hippe, 2017; Skov et al., 2019]. The more
82 common ^{26}Al - ^{10}Be system, which is classically used for burial dating studies, is much less
83 sensitive to fluctuations of denudation on this time frame [Mudd, 2016], but has been
84 shown to offer important insights over longer time scales [Knudsen and Egholm, 2018;
85 Struck et al., 2018], and its actual potential to decipher transient denudation evolution in
86 slow denudation landscapes needs to be explored more systematically.

87 Independent of chronological approaches, another way to characterize transience in land-
88 scapes, resulting from changes in denudation or incision processes, is the study of the
89 imprint of such perturbations on their morphology. Such approaches has been intensively
90 used in fluvial systems , with the analysis of river long-profiles [e.g. Roberts and White,
91 2010; Fox et al., 2015], and the increasing availability of high resolution topographic data
92 has paved the way for similar developments in the hillslope domain [Roering et al., 2007;
93 Hurst et al., 2012, 2013; Grieve et al., 2016b; Mudd, 2016]. Notably, the combination of
94 TCN data with high resolution hillslope morphological analysis has proven to be a fruit-
95 ful source of information on landscape dynamics and their response to past perturbations
96 [Godard et al., 2019].

97 In this study, we investigated the slowly eroding quartzitic landscapes of the Serra do Cipó
98 Range in Minas Gerais, Brazil, by performing both high resolution morphometric analysis
99 and cosmogenic nuclides concentration measurements (^{10}Be and ^{26}Al) at hilltop sites. The
100 observed relationships between these parameters imply an important acceleration of de-
101 nudation over 100s ka timescales and illustrate a new approach to probe into the transient
102 dynamics of landscapes as well as expanding our knowledge of Quaternary paleoclimate of
103 the central-eastern portion of South America.

104 **2 Theoretical background**

105 We present here the key concepts and ideas supporting our analysis of transient hillslope
106 evolution in the Serra do Cipó. As reviewed by Mudd [2016], transient dynamics is a fun-
107 damental attribute of landscapes involving changes in their morphology, sediment fluxes
108 or rates of denudation, and diagnostic observations can be made on these properties to
109 identify such transient state in terms of deviation from morphological or erosional steady
110 states. In the case of hillslopes, insights can be obtained from high resolution morphomet-
111 ric analysis of their shape or from denudation rates calculated from Terrestrial Cosmogenic
112 Nuclides (TCN) concentration measurements in bedrock or stream sediments, which are
113 two types of observations we combine in our study.

114

115 **2.1 Hillslope erosion formulation**

116 Roering et al. [1999] proposed an hillslope transport model, where sediment flux q_s is
117 non-linearly dependant on topographic gradient dz/dx ,

$$q_s = \frac{-K(dz/dx)}{1 - [(dz/dx)/S_c]^2}, \quad (1)$$

118 where K is a transport efficiency, or diffusion, coefficient, z is the elevation of the topo-
119 graphic surface, x the horizontal coordinate and S_c a threshold gradient. Numerous field
120 investigations have supported the validity of this formulation in high relief landscapes [e.g.
121 Ouimet et al., 2009; DiBiase et al., 2010]. In part of the landscape where topographic
122 gradients are small compared to the threshold S_c this relationship can simplify as,

$$q_s = -K \frac{dz}{dx}, \quad (2)$$

123 Equations 1 and 2 are Geomorphic Transport Laws [Dietrich et al., 2003], which can be
124 combined with a continuity statement,

$$\frac{dq_s}{dx} = \beta E, \quad (3)$$

125 with β the rock-to-regolith density ratio and E the long-term denudation rate, which is
126 equal to rock uplift rate when steady state is achieved. Combining equations 2 and 3 yields,

127

$$E = \frac{KC_{HT}}{\beta}, \quad (4)$$

128 where C_{HT} is hilltop curvature, the second-derivative of the topographic surface. Equation
129 4 connects together two fundamental and distinct types of observations, which can be
130 made about landscapes: measurements of their spatial topographic properties, in this case
131 C_{HT} , and measurements of their temporal rate of evolution, in this case erosion rate E .
132 For a given landscape, assessing whether these two types of observations can be reconciled
133 within the framework of equation 4 can be used as a test of the underlying steady-state
134 assumption. It should be noted that equation 4 was derived for the particular case of
135 a ridge-like hillslope system. In the following, we will rather consider isolated hills and
136 a radial symmetry for the hillslopes, which implies a slight modification of equation 4
137 [Anderson, 2002],

$$E = 2\frac{KC_{HT}}{\beta}. \quad (5)$$

138 **2.2 Detection of transience from the confrontation of morpho-** 139 **metric and TCN data**

140 Terrestrial Cosmogenic Nuclides (TCN) are now routinely used for the determination of
141 denudation rates in a variety of settings, as their steady-state concentration C in various

142 materials, such as stream sediment or outcropping bedrock, can be related to denudation
143 rate E with,

$$C = \sum_i \frac{P_i}{\frac{E\rho}{\Lambda_i} + \lambda}, \quad (6)$$

144 with P_i the TCN production rate at the surface, ρ the material density, Λ_i the cosmic ray
145 attenuation length and λ the decay constant for the considered nuclide. Subscripts i refers
146 to the various production pathways, such as spallation by neutrons or muons capture. The
147 integration time scale of these denudation rate measurements is usually calculated as the
148 time required to erode a thickness equivalent to the neutrons attenuation length-scale, or
149 ~ 60 cm in most situations [von Blanckenburg, 2005]. It results in a wide range of integra-
150 tion windows from Ma to ka timescales for denudation rates ranging from 1 to 100 m/Ma,
151 respectively. This dependency of integration time on denudation rates implies that sites
152 with different denudation rates will respond more or less rapidly, in term of TCN-derived
153 denudation rates, to perturbations of similar amplitude, and can be used to identify tran-
154 sient adjustment in landscapes as we illustrate below.

155 If a local cosmogenic nuclides steady state is achieved at the hilltop scale, the relation-
156 ship between denudation rate E and hilltop curvature C_{HT} is linear and set by equation
157 5, assuming a spatially constant value for the sediment transport coefficient K (Fig. 1).
158 Transience resulting from a change in the sediment transport coefficient through time can
159 be detected by the non-alignment of the E vs C_{HT} or $[^{10}\text{Be}]$ vs C_{HT} relationships to the-
160 oretical steady-state predictions. For the case of a slow denudation landscape, we assume
161 that hillslope morphology does not change significantly over a 100 ka time-scale, and do
162 not take into account eventual feedback between denudation and hilltop curvature.

163

164 **2.3 Detection of transience from TCN pairs**

165 As discussed by Mudd [2016], independently of morphological considerations, transience in
166 denudation can also be detected by the use of pairs of cosmogenic nuclides with different
167 decay constants. ^{10}Be - ^{26}Al is the most widely used TCN pair, notably in burial dating
168 applications [Granger and Muzikar, 2001]. However, their decay constant are of the same
169 order of magnitude, which greatly limit the sensitivity of this system for the identification
170 of transient adjustment conditions [Mudd, 2016]. Instead, this has oriented research ef-
171 forts toward the ^{10}Be - ^{14}C pair as the most promising system to resolve recent changes in
172 denudation [Hippe, 2017; Skov et al., 2019; Hippe et al., 2021]. Nevertheless, it should be
173 noted that in the particular case of slowly eroding landscapes, where the ^{10}Be and ^{26}Al
174 half-lives are comparable with the TCN denudation integration timescale, the amplitude of
175 the deviation of isotopic ratio away from steady-state denudation predictions can become
176 analytically resolvable (Fig. 2). This deviation is particularly noticeable for an increase
177 in denudation rate, as it significantly lowers the ratio below the steady-state denudation
178 curve. The time-scale of the perturbation being also dependent on the denudation rate, the
179 transient response can thus be observed over a few 100s ka in the case of slowly evolving
180 landscapes (1 m/Ma).

181 **3 Settings**

182 Our study area is located in the Serra do Cipó national park, in the highlands of the
183 Brazilian Southeast. The Serra do Cipó mountain is a narrow (30-km wide) quartzitic
184 range located in the southern portion of the Espinhaço Range (Fig. 3), which is the most
185 extensive and continuous Precambrian orogenic belt of the South American Platform and
186 originated 600 Ma ago during the Brazilian Orogeny [Magalhães Junior et al., 2015]. The
187 Espinhaço Range is an important hydrographic and landscape divider in South America.

188 To the west is located the large hydrographic basin of the São Francisco River, which drains
189 a craton characterized by smooth relief, semi-humid climate, and savanna vegetation. To
190 the east, drainage is organized around smaller watersheds, such as the Doce and Jequit-
191 inhona hydrographic basins, that drain a half-orange hills plateau-type landscape, under
192 humid climate and tropical forests [Salgado et al., 2019].

193 After its uplift during the Brazilian Orogeny, the Serra do Cipó has not been subjected to
194 new orogenic phases and the subsequent erosion of the range resulted in a relief character-
195 ized by a wide quartzitic plateau (average elevation 1200 m), comprising a large sequence
196 of ridges, reaching 2000 m in altitude, depressions and dissected fluvial valleys. There are
197 no evidence of a direct impact of the opening of the South Atlantic on our study area.
198 Although landscape properties are globally homogeneous across the Serra do Cipó, the
199 portion of the range that drains towards the Doce River is more dissected than that drain-
200 ing into the São Francisco River.

201 Nowadays, the climate of Serra do Cipó Range is mesothermal, with Mean Annual Temper-
202 ature between 18°C-19°C and Mean Annual Precipitation ranging from 1250 to 1550 mm,
203 as well as dry winters and wet summers. However, there are lines of evidence, from pedo-
204 logical and geomorphological records, that the region underwent many climatic changes
205 during the Holocene and late Pleistocene, with occurrences of periods wetter and dryer
206 than the present-day conditions [Chueng et al., 2019; Barros and Magalhães Junior, 2020;
207 Silva et al., 2020].

208 Due to the great resistance of the quartzite bedrock to erosion, denudation rates are <6
209 m/Ma [Barreto et al., 2013; Peifer et al., 2020], soils are thin and poor, hosting the typi-
210 cal vegetation of Campos Rupestres, a high altitude rocky field biome [Magalhães Junior
211 et al., 2015]. This combination of slow denudation rates and significant relief is well suited
212 for the coupling of high-resolution morphometry and cosmogenic nuclides analyses due to
213 long-integration time scales for denudation, a limited contribution of stochastic events to

214 surface processes, a limited storage of erosion products and long relief response timescales.

215 4 Methods

216 4.1 General sampling strategy

217 Our strategy was to select prominent sites on top of soil-mantled vegetation-free hillslopes
218 (Fig. 4), where the observed denudation rates E and morphological properties such as
219 hilltop curvature C_{HT} could be linked into the simple physical framework of equation 5
220 [Anderson, 2002; Hurst et al., 2012]. The slope of this relationship between E and C_{HT} is
221 set by the sediment transport coefficient K and the rock-to-regolith ratio β .

222 We primarily selected regolith-mantled hilltop sites, with regular morphologies and no
223 bedrock outcrops (Fig. 4A-B). We sampled quartz fragments resulting from the disman-
224 tlement of quartz veins embedded in the fine-grained quartzite bedrock and sandy regolith
225 (Fig. 4C). At some sites, the quartz veins were directly outcropping, but not significantly
226 protruding over the surface, and the quartz fragments were detached directly from the
227 veins (Fig. 4D). At other sites, the veins were not directly outcropping, but covered by
228 10 to 20 cm of regolith. We observed that the quartz veins remain coherent and resistant
229 during their exhumation toward the surface, whereas the fine grained quartzite bedrock
230 is converted into sandy regolith. Site O is an exception, where we directly sampled the
231 outcropping quartzite bedrock.

232 4.2 Cosmogenic nuclides analysis

233 Samples for ^{10}Be and ^{26}Al concentrations measurements were collected at 11 hilltop sites,
234 by amalgamating 30 to 40 individual quartz vein fragments at the surface (except for site
235 O). Samples were crushed and sieved to extract the 250-1000 μm fraction, which was sub-

mitted to sequential magnetic separations. The remaining fraction was leached with 37% HCl to remove eventual carbonate fragments. The samples were then repetitively leached with H_2SiF_6 and submitted to vigorous mechanical shaking until pure quartz was obtained. Decontamination from atmospheric ^{10}Be was achieved by a series of three successive leachings in concentrated HF, each removing 10% of the remaining sample mass [Brown et al., 1991]. After addition of Be and Al carriers, the samples were digested in concentrated HF. Be and Al were isolated for measurements using ion-exchange chromatography. $^{10}\text{Be}/^9\text{Be}$ and $^{26}\text{Al}/^{27}\text{Al}$ measurements were performed at the French AMS National Facility, located at CEREGE in Aix-en-Provence. All results and technical characteristics of the measurements and calculations are provided in tables 1 and 2.

For reference, and before investigating time-variations in denudation, we compute steady-state denudation rates (tables 1 and 2), which were calculated with the online calculator described in Balco et al. [2008] and the nuclide specific LSD scaling scheme of Lifton et al. [2014], using the CRONUS-Earth calibration dataset [Borchers et al., 2016] for the calculation of spallation production rates and muon production rates according to Balco [2017]. We used 160 g/cm^2 for the effective neutron attenuation length in rock, and a density of 2.65 g/cm^3 . No shielding correction was considered for the hilltop sites we sampled.

4.3 Morphometric analysis

We acquired a triplet of Pléiades images covering our sampling area (Fig. 3B), and used photogrammetric techniques to construct a 1 m resolution Digital Surface Model (DSM) and perform hilltop curvature calculations. Pléiades satellites provide panchromatic images with a 0.7 m resolution resampled at 0.5 m pixel size, and have the capacity to acquire multi-stereo views of a scene during the same orbit [Bernard et al., 2012]. In low vegetation settings, they provide an efficient and cost-effective alternative to airborne LiDAR to produce high-resolution Digital Elevation Models over large areas [e.g. Ansberque et al.,

261 [2016]. While this type of imagery, and derived topographic data, has been extensively used
262 in tectonic geomorphology investigations since the launch of the satellites in 2011, its use
263 in quantitative process-oriented geomorphological studies is less common [Godard et al.,
264 2019]. A triplet of Pléiades images was acquired by instrument PHR1A on the 5th of July
265 2019 over a ~ 250 km² area, covering the hilltop sites studied here.

266 The image triplet was processed with NASA AMES Stereo pipeline [Broxton and Edwards,
267 2008; Moratto et al., 2010] in order to produce a Digital Surface Model (DSM). We used the
268 Rational Polynom Coefficients (RPC) provided with the images for the internal calibration
269 of the pushbroom sensor. No Ground Control Points were used during the processing. The
270 images were first roughly aligned by orthorectification on WGS84 datum using a SRTM
271 Digital Elevation Model. Low-resolution disparity maps for couples of images were com-
272 puted to determine coarse correspondence between pixels. Sub-pixel refinement was then
273 performed using an adaptive window correlator [Nefian et al., 2009]. The disparity map
274 was filtered by removing pixels with a value differing from the mean of their neighborhood
275 by more than 3. The point cloud was triangulated and gridded to produce a 1-m resolution
276 Digital Surface Model (Figs. 3 and 5).

277 In order to compute hilltop curvature C_{HT} , we fitted a quadratic surface to the DSM el-
278 evation over a circular window centered on the sampling point [Hurst et al., 2012]. The
279 equation of the surface is,

$$z = ax^2 + by^2 + cxy + dx + ey + f. \quad (7)$$

280 Topographic curvature C_{HT} is computed as the two-dimensional Laplacian of the quadratic
281 surface as,

$$C_{HT} = 2a + 2b \quad (8)$$

282 The radius of the analysis window was chosen to be large enough to filter short-wavelength
283 surface roughness, and small enough to avoid perturbation from the ridge-and-valley to-
284 pographic signal [Lashermes et al., 2007; Roering et al., 2010; Hurst et al., 2012; Godard
285 et al., 2016; Grieve et al., 2016a]. In our case, this radius was set at 10 m (Fig. 6). In
286 order to account for uncertainties on the position of the sampling sites and the influence
287 of small wavelength topographic fluctuations, we computed C_{HT} at each pixel within a 10
288 m radius of the sampling point, and then calculated the mean and standard deviation of
289 these values.

290 4.4 Numerical modeling

291 We predicted the concentrations in ^{10}Be and ^{26}Al at the surface by considering the pro-
292 gressive accumulation of these cosmogenic nuclides during exhumation as a response to
293 imposed time-varying denudation, using a Lagrangian point of view [Knudsen et al., 2019].
294 We used the CRONUS-Earth calibration dataset [Borchers et al., 2016] and nuclides specific
295 time-dependent LSD scaling scheme [Lifton et al., 2014], for the calculation of spallation
296 production rates. Muons production was computed following Model 1A and associated
297 parameters from Balco [2017]. We used 160 g/cm^2 for the effective neutron attenuation
298 length in rock, and a density of 2.65 g/cm^3 .

299 The originality of our approach is that the denudation rate E at our sites of interest is
300 computed from their measured hilltop curvature C_{HT} according to equation 5. This al-
301 lows us to impose time-variations in denudation through changes in K , affecting all sites
302 synchronously, rather than considering the evolution of denudation rates at each site indi-
303 vidually. In other words, this allowed us to perform a joint inversion of a single K history
304 to assess the changes in denudation through time, rather than dealing with the 11 inde-
305 pendent denudation histories at each site separately.

306 We parameterized the evolution of the sediment transport coefficient K through time as a

307 two-steps history, which is thus defined by three parameters : (1) the sediment transport
 308 coefficient K_1 during an initial slow denudation phase, (2) the sediment transport coeffi-
 309 cient K_2 during a recent faster denudation phase and (3) the transition time T between the
 310 two phases. Similar scenarios of hillslope evolution based on a two-steps history for the sed-
 311 iment transport coefficient were explored by [Roering et al. \[2004\]](#) over shorter timescales,
 312 and allowed to capture the impact of a climate changing event while limiting the number of
 313 free parameters. A significant amount of scatter is expected in our dataset, which is usual
 314 in the type of complex natural system we are dealing with. Our forward model is based
 315 on a simplified definition of the problem, which does not account for numerous processes
 316 complicating hillslope dynamics and are not captured by idealized relationships such as
 317 equation 5. Additionally, the two-steps scenario we used is a coarse, but necessary, simpli-
 318 fication of the actual denudation history. Such epistemic uncertainty is not represented by
 319 the measurement errors on either the ^{10}Be concentrations or hilltop curvatures. For that
 320 reason, we do not expect the modelled concentrations C_{mod} to be able to fit the observed
 321 concentrations C_{obs} within these measurement errors. We introduce a residual error σ_e as
 322 a 4th parameter which is sampled along the ones described above [[Laloy et al., 2017](#)], with
 323 a likelihood defined as,

$$L(K_1, K_2, T) = \frac{1}{\sqrt{2\pi}\sigma_e} \exp\left(\frac{-1}{2\sigma_e^2} \sum_{i=1}^n (C_{obs,i} - C_{mod,i}(K_1, K_2, T))^2\right), \quad (9)$$

324 where n is the total number of observed TCN concentrations used in the inversion. We used
 325 a standard Monte Carlo-Markov Chain (MCMC) approach to move through the parameter
 326 space and estimate the posterior distributions [[Metropolis et al., 1953](#)].

327 5 Data

328 At hilltops, the measured ^{10}Be concentrations range from 0.8 ± 0.02 to 6.9 ± 0.1 10^6 at/g
329 (Fig. 7A and table 1), which corresponds to steady denudation rates of 6 ± 0.5 to 0.35 ± 0.05
330 m/Ma, respectively. The $^{26}\text{Al}/^{10}\text{Be}$ ratios range from 4.4 ± 0.1 to 6.4 ± 0.2 , with 6 samples
331 plotting within the erosion island, slightly above the steady state erosion curve (Fig. 7A
332 and table 2). These samples are evenly distributed over the range of observed ^{10}Be con-
333 centrations. One sample (R) presents an anomalously high ratio, which is impossible to
334 obtain by TCN accumulation and decay. It is probably affected by an analytical issue on
335 the determination of the ^{27}Al concentration, which is significantly higher than the rest of
336 the dataset (except sample O). Only the ^{10}Be concentration will be used for this sample
337 in the following. Finally, 4 samples display ratios clearly below steady-state denudation
338 predictions, including the 3 samples with the lowest ^{10}Be concentrations.

339 At our sampling sites, measured hilltop curvatures span an order of magnitude from 0.005
340 to 0.039 m^{-1} (Fig. 7B and table 3). Denudation rates, calculated under a steady state
341 assumption, increase with hilltop curvature. We note that sample O is slightly off the gen-
342 eral trend and corresponds to the only site where we sampled the outcropping quartzite
343 bedrock, instead of the quartz veins.

344 6 Discussion

345 6.1 Interpretation of observed TCN concentrations

346 The denudation rates calculated under a steady-state assumption span a large range, from
347 0.5 to 6 m/Ma. Barreto et al. [2013] reported denudation rates of 1.8 to 2.4 m/Ma and 4.0 to
348 6.3 m/Ma for catchments located in the São Francisco and Doce river basins, respectively.
349 The global range of denudation rates reported for these catchment wide denudation rates

350 is largely overlapping with our local measurements near the drainage divide. We do not
351 observe systematic gradient in denudation rates at our sites between the two sides of the
352 divide, as in the results of [Barreto et al., 2013], and the diversity of denudation rates in
353 our dataset probably reflects an underlying long-standing diversity in hillslope and hilltop
354 morphologies across the relict landscape of the Serra do Cipó uplands.

355 Some of our samples present $^{26}\text{Al}/^{10}\text{Be}$ ratios that are significantly lower than steady-state
356 denudation predictions (sites Q, M, U and V). Such low ratios are usually interpreted
357 as reflecting temporary burial of the material [Granger and Muzikar, 2001] where, in the
358 absence of TCN production, the differential rate of decay between the two isotopes is
359 progressively lowering the ratio. However, such explanation is highly unlikely for our
360 samples collected at the top of continuously eroding prominent hilltop sites, where there is
361 no evidence for any significant potential for long-term storage and burial. Regolith mixing
362 in slowly eroding soil profiles can also induce a lowering of $^{26}\text{Al}/^{10}\text{Be}$ ratios below the
363 steady-state denudation line [e.g. Makhubela et al., 2019]. While this process could explain
364 the measured ratio at site Q, it is difficult to reconcile with field observations at the other
365 sites where we directly sampled outcropping veins. Furthermore, these three sites (M, U
366 and V) display the highest denudation rates, and are eroding almost an order of magnitude
367 faster than the slowest sites of the dataset. The last possible process to explain the observed
368 low $^{26}\text{Al}/^{10}\text{Be}$ ratios at sites M, U and V is an increase of denudation rate [Struck et al.,
369 2018], which would dominantly impact the fastest sites with short integration time scales
370 (100-200 ka, table 1) and much less the slowest sites, which average denudation over a longer
371 time-frame (Fig. 2). Independent of any consideration on the morphology of the studied
372 sites, our TCN data present evidence of transience and acceleration of denudation rates in
373 the past. The amplitude and timing of such increase is however difficult to constrain from
374 ^{26}Al - ^{10}Be data alone.

6.2 Relationship between TCN data and hilltop morphology

The relationship between denudation rate E and hilltop curvature C_{HT} (equation 5) is not linear (Fig. 7B), as would be expected from hillslope diffusion theory [Anderson, 2002; Hurst et al., 2012]. No single sediment transport coefficient can explain the data within uncertainty, and we observe a systematic tendency for the sites with higher denudation rates (lower integration time scale) to plot on a higher K line, when compared to the slower ones. In line with our previous observations on the $^{26}\text{Al}/^{10}\text{Be}$ ratios, this constitutes an additional evidence for an acceleration of denudation over our area of interest (Fig. 1). We note that a recent large-scale compilation by Gabet et al. [2021] have also identified non-linearity in the relationship between C_{HT} and TCN-derived denudation rates but further investigations are needed to assess its signification in terms of hillslope dynamics.

In order to obtain more quantitative insights on this postulated acceleration of denudation, we tested a 2-stage denudation history defined by 3 parameters : the transition time between the slow and fast periods of denudation and their respective sediment transport coefficients (Fig. 8). We predicted ^{10}Be concentrations at the sites of interest for any combinations of these parameters, using the measured hilltop curvature (C_{HT}) to compute denudation rates evolution through time using equation 5, and perform a MCMC driven inversion. The sampling of the parameter space is driven by the Metropolis-Hasting algorithm, with an acceptance rate of 32%. We ran 16 independent chains, each 5×10^5 , in length with a 10^4 length burn-in phase. The multivariate Potential Scale Reduction Factor is 1.001 suggesting convergence was achieved [Gelman and Rubin, 1992].

The inversion results support a low initial K value ($< 8 \times 10^{-5} \text{ m}^2/\text{a}$), followed by a very marked increase (5×10^{-5} to $5 \times 10^{-4} \text{ m}^2/\text{a}$). A pronounced trade-off exists between the onset time of the second phase and the value of its sediment transport coefficient, which makes it difficult to directly confront these results with climatological and morphological records. Indeed, both an intense and recent phase with a transition as young as 10 ka or

401 a much older up to 1 Ma event with lower sediment transport coefficient could provide
402 reasonable fits to the data (Fig. 8B). We note that solving for TCN accumulation using an
403 simplified Eulerian approach [Knudsen et al., 2019] with exponential attenuation profile for
404 muonic production and a time-independent scaling [Stone, 2000], instead of the Lagrangian
405 scheme we used in our reference model, does not substantially modify the outcome of the
406 inversion (Fig. 9B).

407 Additional independent constraints can be obtained from the low $^{26}\text{Al}/^{10}\text{Be}$ ratios of the
408 fastest denudation sites. Assuming an initial $K_1 = 4 \times 10^{-5} \text{ m}^2/\text{a}$, for each value of K_2 we
409 computed the best transition time T allowing to explain both ^{10}Be and ^{26}Al concentra-
410 tions within 1σ uncertainty, for each sample independently (Fig. 8A, red lines). For each
411 of these samples (M, U, V), we observed the same tradeoff between K_2 and T as for the
412 C_{HT} - ^{10}Be inversion of the whole dataset. The lines defining the best K_2 - T combinations
413 for these ^{26}Al - ^{10}Be data appears to intersect the region of maximum posterior density for
414 the C_{HT} - ^{10}Be inversion at a transition time $T \sim 100 \text{ ka}$. Finally, a joint inversion of C_{HT} ,
415 ^{10}Be and ^{26}Al data for the whole dataset narrows down the range of probable transition
416 time and is also consistent with a value close to 100 ka (Fig. 9C). As discussed below,
417 this time scale for a postulated shift in surface dynamics is in agreement with reported
418 environmental changes in the area, notably precipitation [e.g. Cruz et al., 2009b].

419 We note that our results could be affected by the processes occurring during the exhumation
420 of the quartz fragments sampled at the surface. Notably, a mixing of these fragments in the
421 regolith layer, rather than the monotonous exhumation toward the surface assumed in our
422 models, would significantly impact their accumulation of cosmogenic nuclides through time
423 [Granger et al., 1996; Makhubela et al., 2019]. As discussed above, we have numerous lines
424 of evidence that those fragments result from the dismantlement of massive quartz veins,
425 which remained mostly cohesive during their exhumation history embedded in the regolith,
426 implying little mixing. The $^{26}\text{Al}/^{10}\text{Be}$ ratios of most of the high-concentration samples are

427 not compatible with a significant mixing of the fragments in the regolith (Fig 7A), with the
428 exception of sample Q. We also note that our reference model is designed with a constant
429 density during the exhumation history. In order to test the influence of a change in density
430 when moving through the regolith for the final stage of exhumation [Struck et al., 2018],
431 we tested the effect of a 1-m thick layer of density 1.7, and we observed that such mod-
432 ification does not substantially alter the general pattern retrieved from the inversion for
433 the various parameters (Fig. 9D). It is important to note that our approach relies on the
434 hypothesis that hillslope morphology does not change substantially over the investigated
435 time period, so that there is no feedback between denudation and hilltop curvature, which
436 is considered constant here. Calculated hillslope response times for the range of very low
437 denudation rates and sediment transport coefficient considered here are at least several
438 Ma, supporting the hypothesis of a stable landscape over the time-frame of the climatic
439 perturbations scenarios we investigate (Fig. 10).

440 **6.3 Comparison with regional climatic and geomorphic records**

441 The two types of observations we made (C_{HT} - ^{10}Be relationship and $^{26}\text{Al}/^{10}\text{Be}$ ratios) sug-
442 gest a significant increase of denudation occurring over the last few 100s ka. However, it
443 is difficult to pinpoint an actual event from each approach alone. Indeed, onset of rapid
444 denudation as young as a few 10s ka, close to the Last Glacial Maximum, or as old as
445 800 ka, near the Mid-Pleistocene Transition, provide comparable fits to the C_{HT} - ^{10}Be data
446 (Fig. 8). We note that we also used a very simplified 3-parameters definition of the evolu-
447 tion of K , which implies a single step-change and does not allow the possibility of multiple
448 events or of a gradual change. We tested this type of scenario by mapping the evolution of
449 the sediment transport coefficient on the $\delta^{18}\text{O}$ stack of Lisiecki and Raymo [2005], with a
450 prescribed range of variations. Such evolution of K yields a relationship between C_{HT} and
451 ^{10}Be concentrations that does not fit the data as well as the abrupt evolution associated

452 with the 3-parameters scenarios. However, it still reproduces the general trend and in
453 particular the fact that it does not correspond to a steady state situation (Fig. 8C, green
454 line). When considered alone, the $^{26}\text{Al}/^{10}\text{Be}$ ratios of the high-denudation samples also
455 display a similar tradeoff between T and K_2 , but the combination with C_{HT} - ^{10}Be inversion
456 results significantly narrows down the range of likely age for the onset of the increase in
457 denudation rates to 100-300 ka (Figs. 8 and S4).

458 There are lines of evidence supporting important Quaternary fluctuations of precipitation,
459 temperature and vegetation in SE Brazil [Salgado-Labouriau et al., 1998; Behling, 2002;
460 Ledru et al., 2005], and in particular in the Espinhaço Range [Chueng et al., 2019; Silva
461 et al., 2020]. For example, precipitation has been shown to be strongly modulated by
462 orbital fluctuations [Wang et al., 2007; Cruz et al., 2009a], with some speleothem records
463 suggesting a wetter climate starting at 70 ka [Cruz et al., 2009b], a timing comparable
464 with the transition time inferred from our inversion results. Early and Middle Quater-
465 nary geomorphological markers, such as river terraces, are often poorly preserved in the
466 area, but display a strong climatic control on cycles of erosion and deposition [Barros and
467 Magalhães Junior, 2020]. The hypothesis that climatic fluctuations is the main driver of
468 the increase in denudation rates is reinforced by the fact that there was a reduction in in-
469 traplate tectonic activity beginning in the Middle Quaternary or earlier in the southeastern
470 highlands of Brazil [Salgado et al., 2016]. This idea of a dominant climatic control is further
471 reinforced by the non-linear E - C_{HT} relationship observed in figure 7, which can be consid-
472 ered as symptomatic of a top-down climatic forcing, where climatically-triggered changes in
473 precipitation or vegetation modulate hillslope sediment transport coefficient. Conversely, a
474 bottom-up perturbation associated with tectonically-driven base level changes would pre-
475 serve the co-linearity of the samples in an E - C_{HT} plot. While we cannot unambiguously
476 associate a particular event to our observations of transience in the landscape of the Serra
477 do Cipó, they probably result from the integration of climatic fluctuations and an increased

478 denudation trend over the Late Pleistocene.

479 **6.4 Implications for the detection of transient evolution in land-** 480 **scapes**

481 Combining the analysis of detailed high resolution hillslope morphometry with TCN data
482 is a promising way to investigate landscape dynamics but has been only used in a limited
483 number of situations [DiBiase et al., 2012; Hurst et al., 2012; Godard et al., 2019, 2020].
484 Such an approach allows to combine the two types of observation into a physical, process-
485 based framework, such as equation 5, in order to test the underlying assumption and
486 evaluate its limitations. Our study illustrates the potential of such an approach to identify
487 transient dynamics in slowly eroding landscapes, and assess its links with climatically-
488 driven top-down forcings. We take advantage of the differences in integration timescales of
489 the two methods: a few 100 ka for TCN concentrations and of the order of 1 Ma for hilltop
490 curvature measurements (Fig. 10), which allows to unravel time variations in the intensity
491 of surface processes. Hilltops of the Serra do Cipó range display several evidences of Late
492 Quaternary acceleration of erosion, as the relationship between ^{10}Be concentrations and
493 hilltop morphology, as well as the $^{26}\text{Al}/^{10}\text{Be}$ ratios, both displaying significant deviation
494 from steady state predictions. There are however limits to the resolving power of such com-
495 bination with respect to the details of denudation history that can be retrieved, which are
496 manifest in the observed trade-offs between parameters (Fig 8A and 9). Using additional
497 TCN, such ^{36}Cl or *in situ* ^{14}C might allow to extract more details about the denudation
498 history. However, *in situ* ^{14}C has not yet been used to investigate such low denudation
499 settings and modeling studies anticipate important limitations to its resolving power in
500 such settings [Skov et al., 2019]. ^{36}Cl would require target minerals such as carbonates
501 or feldspars which are not present in the setting we investigated, but might be feasible in

502 granitic landscapes. While it does not provide a time-series for the evolution of denuda-
503 tion, our study illustrates the possibilities and potential of investigating paleo-denudation
504 of slowly evolving landscapes in addition to the often explored tectonically active mountain
505 ranges.

506 **7 Conclusion**

507 We studied the denudation of hilltop sites in the Serra do Cipó range, by collecting high
508 resolution morphometric data and measuring ^{10}Be and ^{26}Al concentrations in surface mate-
509 rials. We compared our observations with prediction of simple hillslope diffusion theory for
510 the relationship between morphological attributes and denudation rates derived from these
511 TCN concentrations. We identified substantial deviation from steady state configuration,
512 suggesting an important change in surface denudation over recent time periods, which re-
513 sults in the observed transient state. The originality of our approach is to conduct a joint
514 inversion of both isotopic and morphometric data to derive the temporal evolution of the
515 hillslope sediment transport coefficient. Our inversions suggest an important increase in
516 the sediment transport coefficient and denudation rate over 100 ka timescale, which most
517 likely results from a modulation of soil transport efficiency of climatic origin. However, a
518 trade-off between the timing of the acceleration and denudation intensity limits our ability
519 to precisely pin point a specific climatic event. Our study illustrates the strong poten-
520 tial of landscape analysis that link geochronological and topographic data into a single
521 physically-based framework, as for example hillslope diffusion theory. In our case, it allows
522 to identify transient dynamics at the scale of hillslope, and the persistence of instabilities,
523 which is key for longer-wavelength landscape-scale analysis of the influence of climatic and
524 tectonic forcings.

Acknowledgments

This work was supported by CAPES-COFECUB (Research Project 869/15) and an IUF fellowship to VG. The ^{10}Be and ^{26}Al measurements were performed at the ASTER AMS national facility (CEREGE, Aix en Provence) which is supported by the INSU/CNRS, the ANR through the "Projets thématiques d'excellence" program for the "Equipements d'excellence" ASTER-CEREGE action and IRD. We thank Rodolphe Cattin for insightful discussions. Constructive comments by Simon Mudd, an anonymous reviewer and the associate editor greatly helped to improve this manuscript. This article is dedicated to the memory of our friend and colleague Didier L. Bourlès who sadly passed away during its preparation.

References

- Anderson, R. S. (2002). Modeling the tor-dotted crests, bedrock edges, and parabolic profiles of high alpine surfaces of the Wind River Range, Wyoming. *Geomorphology*, 46(1-2):35–58.
- Ansberque, C., Bellier, O., Godard, V., Lasserre, C., Wang, M., Braucher, R., Talon, B., de Sigoyer, J., Xu, X., and Bourlès, D. L. (2016). The Longriqu fault zone, eastern Tibetan Plateau: Segmentation and Holocene behavior. *Tectonics*, 35(3):565–585.
- Arnold, M., Merchel, S., Bourlès, D. L., Braucher, R., Benedetti, L., Finkel, R. C., Aumaître, G., Gottdang, A., and Klein, M. (2010). The French accelerator mass spectrometry facility ASTER: Improved performance and developments. *Nuclear Instruments and Methods in Physics Research, Section B: Beam Interactions with Materials and Atoms*, 268(11-12):1954–1959. ISBN: 0168-583X.
- Balco, G. (2017). Production rate calculations for cosmic-ray-muon-produced ^{10}Be and ^{26}Al benchmarked against geological calibration data. *Quaternary Geochronology*, 39:150–173. Publisher: Elsevier B.V.
- Balco, G., Stone, J. O., Lifton, N. a., and Dunai, T. J. (2008). A complete and easily accessible means of calculating surface exposure ages or erosion rates from ^{10}Be and ^{26}Al measurements. *Quaternary Geochronology*, 3(3):174–195. ISBN: 1871-1014.
- Barreto, H. N., Varajão, C. A., Braucher, R., Bourlès, D. L., Salgado, A. A., and Varajão, A. F. (2013). Denudation rates of the Southern Espinhaço Range, Minas Gerais, Brazil, determined by in situ-produced cosmogenic beryllium-10. *Geomorphology*, 191:1–13.

- 556 Barros, L. F. d. P. and Magalhães Junior, A. P. (2020). Late quaternary landscape evolution
557 in the Atlantic Plateau (Brazilian highlands): Tectonic and climatic implications of
558 fluvial archives. *Earth-Science Reviews*, 207(May):103228. Publisher: Elsevier.
- 559 Behling, H. (2002). South and southeast Brazilian grasslands during Late Quaternary
560 times: A synthesis. *Palaeogeography, Palaeoclimatology, Palaeoecology*, 177(1-2):19–27.
- 561 Bernard, M., Decluseau, D., Gabet, L., and Nonin, P. (2012). 3D capabilities of PLEIADES
562 satellite. *ISPRS - International Archives of the Photogrammetry, Remote Sensing and*
563 *Spatial Information Sciences*, XXXIX-B3:553–557.
- 564 Borchers, B., Marrero, S., Balco, G., Caffee, M., Goehring, B., Lifton, N., Nishiizumi,
565 K., Phillips, F., Schaefer, J., and Stone, J. (2016). Geological calibration of spallation
566 production rates in the CRONUS-Earth project. *Quaternary Geochronology*, 31:188–198.
567 Publisher: Elsevier B.V ISBN: 4025594390.
- 568 Braucher, R., Guillou, V., Bourlès, D. L., Arnold, M., Aumâtre, G., Keddadouche, K.,
569 and Nottoli, E. (2015). Preparation of ASTER in-house $^{10}\text{Be}/^{9}\text{Be}$ standard solutions.
570 *Nuclear Instruments and Methods in Physics Research Section B: Beam Interactions*
571 *with Materials and Atoms*, 361:335–340.
- 572 Braucher, R., Merchel, S., Borgomano, J., and Bourlès, D. (2011). Production of cosmo-
573 genic radionuclides at great depth: A multi element approach. *Earth and Planetary*
574 *Science Letters*, 309(1-2):1–9.
- 575 Brown, E. T., Edmond, J. M., Raisbeck, G. M., Yiou, F., Kurz, M. D., and Brook,
576 E. J. (1991). Examination of surface exposure ages of Antarctic moraines using in situ
577 produced ^{10}Be and ^{26}Al . *Geochimica et Cosmochimica Acta*, 55(8):2269–2283. ISBN:
578 0016-7037.
- 579 Broxton, M. and Edwards, L. (2008). The Ames Stereo Pipeline: Automated 3D Surface
580 Reconstruction from Orbital Imagery. In *Lunar and Planetary Science Conference*,
581 volume 39, page 2419, League City, Texas. Series Title: Lunar and Planetary Science
582 Conference.
- 583 Champagnac, J.-D., Molnar, P., Sue, C., and Herman, F. (2012). Tectonics, climate, and
584 mountain topography. *Journal of Geophysical Research*, 117(B2):B02403.
- 585 Charreau, J., Blard, P.-H., Puchol, N., Avouac, J.-P., Lallier-Vergès, E., Bourlès, D.,
586 Braucher, R., Gallaud, A., Finkel, R., Jolivet, M., Chen, Y., and Roy, P. (2011). Paleo-
587 erosion rates in Central Asia since 9Ma: A transient increase at the onset of Quaternary
588 glaciations? *Earth and Planetary Science Letters*, 304(1-2):85–92.
- 589 Chueng, K. F., Gomes Coe, H. H., Ribeiro Rocha Augustin, C. H., Macario, K. D.,
590 Fricks Ricardo, S. D., and Carvalho Vasconcelos, A. M. (2019). Landscape paleody-
591 namics in siliciclastic domains with the use of phytoliths, sponge spicules and carbon

- 592 isotopes: The case of southern Espinhaço Mountain Range, Minas Gerais, Brazil. *Journal of South American Earth Sciences*, 95(April):102232. Publisher: Elsevier.
- 593
- 594 Cruz, F. W., Vuille, M., Burns, S. J., Wang, X., Cheng, H., Werner, M., Lawrence Edwards,
595 R., Karmann, I., Auler, A. S., and Nguyen, H. (2009a). Orbitally driven east-west an-
596 tiphasing of South American precipitation. *Nature Geoscience*, 2(3):210–214. Publisher:
597 Nature Publishing Group.
- 598 Cruz, F. W., Wang, X., Auler, A., Vuille, M., Burns, S. J., Edwards, L. R., Karmann, I.,
599 and Cheng, H. (2009b). Orbital and Millennial-Scale Precipitation Changes in Brazil
600 from Speleothem Records. In Vimeux, F., Sylvestre, F., and Khodri, M., editors, *Past*
601 *Climate Variability in South America and Surrounding Regions*, volume 14, pages 29–
602 60. Springer Netherlands, Dordrecht. Series Title: Developments in Paleoenvironmental
603 Research.
- 604 DiBiase, R. A., Heimsath, A. M., and Whipple, K. X. (2012). Hillslope response to tectonic
605 forcing in threshold landscapes. *Earth Surface Processes and Landforms*, 37(8):855–865.
- 606 DiBiase, R. A., Whipple, K. X., Heimsath, A. M., and Ouimet, W. B. (2010). Landscape
607 form and millennial erosion rates in the San Gabriel Mountains, CA. *Earth and Planetary*
608 *Science Letters*, 289(1-2):134–144.
- 609 Dietrich, W. E., Bellugi, D. G., Sklar, L. S., Stock, J. D., Heimsath, A. M., and Roering,
610 J. J. (2003). Geomorphic transport laws for predicting landscape form and dynamics.
611 In Wilcock, P. R. and Iverson, R. M., editors, *Prediction in Geomorphology*, volume
612 135, pages 103–132. American Geophysical Union, Washington, D. C. Series Title:
613 Geophysical Monograph Series ISSN: 0065-8448.
- 614 Foster, M. A., Anderson, R. S., Wyshnytzky, C. E., Ouimet, W. B., and Dethier, D. P.
615 (2015). Hillslope lowering rates and mobile-regolith residence times from in situ and
616 meteoric ^{10}Be analysis, Boulder Creek Critical Zone Observatory, Colorado. *Geological*
617 *Society of America Bulletin*, 127(5):862–878.
- 618 Fox, M., Bodin, T., and Shuster, D. L. (2015). Abrupt changes in the rate of Andean
619 Plateau uplift from reversible jump Markov Chain Monte Carlo inversion of river profiles.
620 *Geomorphology*, 238:1–14. Publisher: Elsevier B.V.
- 621 Gabet, E. J., Burbank, D. W., Pratt-Sitaula, B., Putkonen, J., and Bookhagen, B. (2008).
622 Modern erosion rates in the High Himalayas of Nepal. *Earth and Planetary Science*
623 *Letters*, 267(3-4):482–494. ISBN: 0012-821X.
- 624 Gabet, E. J., Mudd, S. M., Wood, R. W., Grieve, S. W. D., Binnie, S. A., and Dunai,
625 T. J. (2021). Hilltop Curvature Increases with the Square Root of Erosion Rate.
626 *Journal of Geophysical Research: Earth Surface*, n/a(n/a):e2020JF005858. _eprint:
627 <https://onlinelibrary.wiley.com/doi/pdf/10.1029/2020JF005858>.

- 628 Gaillardet, J., Dupré, B., Louvat, P., and Allègre, C. (1999). Global silicate weathering and
629 CO₂ consumption rates deduced from the chemistry of large rivers. *Chemical Geology*,
630 159(1-4):3–30.
- 631 Gelman, A. and Rubin, D. B. (1992). Inference from Iterative Simulation Using Multiple
632 Sequences. *Statistical Science*, 7(4):457–472. arXiv: 1011.1669 ISBN: 0883-4237.
- 633 Godard, V., Dosseto, A., Fleury, J., Bellier, O., Siame, L., and ASTER, T. (2019). Tran-
634 sient landscape dynamics across the Southeastern Australian Escarpment. *Earth and*
635 *Planetary Science Letters*, 506:397–406. Publisher: Elsevier B.V.
- 636 Godard, V., Hippolyte, J.-C., Cushing, E., Espurt, N., Fleury, J., Bellier, O., and Ollivier,
637 V. (2020). Hillslope denudation and morphologic response to a rock uplift gradient.
638 *Earth Surface Dynamics*, 8(2):221–243.
- 639 Godard, V., Ollivier, V., Bellier, O., Miramont, C., Shabanian, E., Fleury, J., Benedetti, L.,
640 and Guillou, V. (2016). Weathering-limited hillslope evolution in carbonate landscapes.
641 *Earth and Planetary Science Letters*, 446:10–20. Publisher: Elsevier B.V.
- 642 Granger, D. E., Kirchner, J. W., and Finkel, R. (1996). Spatially averaged long-term
643 erosion rates measured from in situ-produced cosmogenic nuclides in alluvial sediment.
644 *The Journal of Geology*, 104(3):249–257.
- 645 Granger, D. E. and Muzikar, P. F. (2001). Dating sediment burial with in situ-produced
646 cosmogenic nuclides: theory, techniques, and limitations. *Earth and Planetary Science*
647 *Letters*, 188(1-2):269–281. ISBN: 0012-821X.
- 648 Grieve, S. W., Mudd, S. M., and Hurst, M. D. (2016a). How long is a hillslope? *Earth*
649 *Surface Processes and Landforms*, 41(8):1039–1054.
- 650 Grieve, S. W. D., Mudd, S. M., Hurst, M. D., and Milodowski, D. T. (2016b). A nondi-
651 mensional framework for exploring the relief structure of landscapes. *Earth Surface*
652 *Dynamics*, 4(2):309–325.
- 653 Hales, T. C. and Roering, J. J. (2005). Climate-controlled variations in scree production,
654 Southern Alps, New Zealand. *Geology*, 33(9):701–704.
- 655 Herman, F. and Champagnac, J.-D. (2016). Plio-Pleistocene increase of erosion rates in
656 mountain belts in response to climate change. *Terra Nova*, 28(1):2–10.
- 657 Hippe, K. (2017). Constraining processes of landscape change with combined in situ cosmo-
658 genic 14 C- 10 Be analysis. *Quaternary Science Reviews*, 173:1–19. Publisher: Elsevier
659 Ltd.
- 660 Hippe, K., Jansen, J. D., Skov, D. S., Lupker, M., Ivy-Ochs, S., Kober, F., Zeilinger, G.,
661 Capriles, J. M., Christl, M., Maden, C., Vockenhuber, C., and Egholm, D. L. (2021).

- 662 Cosmogenic in situ ^{14}C - ^{10}Be reveals abrupt Late Holocene soil loss in the Andean Al-
663 tiplano. *Nature Communications*, 12(1):2546. Number: 1 Publisher: Nature Publishing
664 Group.
- 665 Hurst, M. D., Mudd, S. M., Attal, M., and Hilley, G. (2013). Hillslopes record the growth
666 and decay of landscapes. *Science*, 341(6148):868–871.
- 667 Hurst, M. D., Mudd, S. M., Walcott, R., Attal, M., and Yoo, K. (2012). Using hilltop
668 curvature to derive the spatial distribution of erosion rates. *Journal of Geophysical
669 Research*, 117(F2):F02017.
- 670 Knudsen, M. F. and Egholm, D. L. (2018). Constraining Quaternary ice covers and erosion
671 rates using cosmogenic $^{26}\text{Al}/^{10}\text{Be}$ nuclide concentrations. *Quaternary Science Reviews*,
672 181:65–75. Publisher: Elsevier Ltd.
- 673 Knudsen, M. F., Egholm, D. L., and Jansen, J. D. (2019). Time-integrating cosmogenic nu-
674 clide inventories under the influence of variable erosion, exposure, and sediment mixing.
675 *Quaternary Geochronology*, 51(December 2018):110–119. Publisher: Elsevier.
- 676 Laloy, E., Beerten, K., Vanacker, V., Christl, M., Rogiers, B., and Wouters, L. (2017).
677 Bayesian inversion of a CRN depth profile to infer Quaternary erosion of the northwestern
678 Campine Plateau (NE Belgium). *Earth Surface Dynamics*, 5(3):331–345.
- 679 Lashermes, B., Foufoula-Georgiou, E., and Dietrich, W. E. (2007). Channel network ex-
680 traction from high resolution topography using wavelets. *Geophysical Research Letters*,
681 34(23):L23S04. ISBN: 0094-8276.
- 682 Ledru, M. P., Rousseau, D. D., Cruz, F. W., Riccomini, C., Karmann, I., and Martin, L.
683 (2005). Paleoclimate changes during the last 100,000 yr from a record in the Brazil-
684 ian Atlantic rainforest region and interhemispheric comparison. *Quaternary Research*,
685 64(3):444–450.
- 686 Lenard, S. J., Lavé, J., France-Lanord, C., Aumaître, G., Boulès, D. L., and Keddadouche,
687 K. (2020). Steady erosion rates in the Himalayas through late Cenozoic climatic changes.
688 *Nature Geoscience*, 13(6):448–452. Publisher: Springer US.
- 689 Lifton, N., Sato, T., and Dunai, T. J. (2014). Scaling in situ cosmogenic nuclide produc-
690 tion rates using analytical approximations to atmospheric cosmic-ray fluxes. *Earth and
691 Planetary Science Letters*, 386:149–160. Publisher: Elsevier B.V.
- 692 Lisiecki, L. E. and Raymo, M. E. (2005). A Pliocene-Pleistocene stack of 57 globally
693 distributed benthic $\delta^{18}\text{O}$ records. *Paleoceanography*, 20(1):PA1003. Publisher: American
694 Geophysical Union.
- 695 Magalhães Junior, A. P., de Paula Barros, L. F., and Felipe, M. F. (2015). Southern Serra
696 do Espinhaço: The Impressive Plateau of Quartzite Ridges. In Vieira, B. C., Salgado, A.

- 697 A. R., and Santos, L. J. C., editors, *Landscapes and landforms of Brazil*, pages 359–370.
698 Springer. ISSN: 22132104.
- 699 Makhubela, T., Kramers, J., Scherler, D., Wittmann, H., Dirks, P., and Winkler, S. (2019).
700 Effects of long soil surface residence times on apparent cosmogenic nuclide denudation
701 rates and burial ages in the Cradle of Humankind, South Africa. *Earth Surface Processes
702 and Landforms*, 44(15):2968–2981.
- 703 Merchel, S., Arnold, M., Aumaître, G., Benedetti, L., Bourlès, D., Braucher, R., Alfimov,
704 V., Freeman, S., Steier, P., and Wallner, A. (2008). Towards more precise ^{10}Be and
705 ^{36}Cl data from measurements at the 10-14 level: Influence of sample preparation. *Nu-
706 clear Instruments and Methods in Physics Research Section B: Beam Interactions with
707 Materials and Atoms*, 266(22):4921–4926.
- 708 Merchel, S. and Bremser, W. (2004). First international ^{26}Al interlaboratory compari-
709 son - Part I. *Nuclear Instruments and Methods in Physics Research Section B: Beam
710 Interactions with Materials and Atoms*, 223-224:393–400. Publisher: North-Holland.
- 711 Metropolis, N., Rosenbluth, A. W., Rosenbluth, M. N., Teller, A. H., and Teller, E. (1953).
712 Equation of State Calculations by Fast Computing Machines. *The Journal of Chemical
713 Physics*, 21(6):1087–1092.
- 714 Moratto, Z., Broxton, M., Beyer, R., Lundy, M., and Husmann, K. (2010). Ames Stereo
715 Pipeline, NASA’s Open Source Automated Stereogrammetry Software. In *Lunar and
716 Planetary Science Conference*, volume 41, page 2364, The Woodlands, Texas. Series
717 Title: Lunar and Planetary Science Conference.
- 718 Mudd, S. M. (2016). Detection of transience in eroding landscapes. *Earth Surface Processes
719 and Landforms*, 42(1):24–41. ISBN: 0197-9337.
- 720 Nefian, A. V., Husmann, K., Broxton, M., To, V., Lundy, M., and Hancher, M. D. (2009).
721 A bayesian formulation for sub-pixel refinement in stereo orbital imagery. In *2009 16th
722 IEEE International Conference on Image Processing (ICIP)*, pages 2361–2364, Cairo,
723 Egypt. IEEE.
- 724 Norton, K. P. and Schlunegger, F. (2017). Lack of a weathering signal with increased
725 Cenozoic erosion? *Terra Nova*, 29(5):265–272.
- 726 Ouimet, W. B., Whipple, K. X., and Granger, D. E. (2009). Beyond threshold hillslopes:
727 Channel adjustment to base-level fall in tectonically active mountain ranges. *Geology*,
728 37(7):579–582. Publisher: Geological Society of America.
- 729 Peifer, D., Persano, C., Hurst, M. D., Bishop, P., and Fabel, D. (2020). Growing topography
730 due to contrasting rock types in a tectonically dead landscape. *Earth Surface Dynamics
731 Discussions*, 2020:1–29.

- 732 Roberts, G. G. and White, N. (2010). Estimating uplift rate histories from river profiles
733 using African examples. *Journal of Geophysical Research*, 115(B2):B02406.
- 734 Roering, J. J., Almond, P., Tonkin, P., and McKean, J. (2004). Constraining climatic
735 controls on hillslope dynamics using a coupled model for the transport of soil and trac-
736 ers: Application to loess-mantled hillslopes, South Island, New Zealand. *Journal of*
737 *Geophysical Research*, 109(F1):F01010. ISBN: 0148-0227.
- 738 Roering, J. J., Kirchner, J. W., and Dietrich, W. E. (1999). Evidence for nonlinear,
739 diffusive sediment transport on hillslopes and implications for landscape morphology.
740 *Water Resources Research*, 35(3):853–870. Publisher: American Geophysical Union.
- 741 Roering, J. J., Kirchner, J. W., and Dietrich, W. E. (2001). Hillslope evolution by nonlin-
742 ear, slope-dependent transport: Steady state morphology and equilibrium adjustment
743 timescales. *Journal of Geophysical Research*, 106(B8):16499–16513. ISBN: 0148-0227.
- 744 Roering, J. J., Marshall, J., Booth, A. M., Mort, M., and Jin, Q. (2010). Evidence for
745 biotic controls on topography and soil production. *Earth and Planetary Science Letters*,
746 298(1-2):183–190. Publisher: Elsevier B.V. ISBN: 0012-821X.
- 747 Roering, J. J., Perron, J. T., and Kirchner, J. W. (2007). Functional relationships between
748 denudation and hillslope form and relief. *Earth and Planetary Science Letters*, 264(1-
749 2):245–258.
- 750 Salgado, A. A. R., Rezende, E. d. A., Bourlès, D., Braucher, R., da Silva, J. R., and Garcia,
751 R. A. (2016). Relief evolution of the Continental Rift of Southeast Brazil revealed by in
752 situ-produced ^{10}Be concentrations in river-borne sediments. *Journal of South American*
753 *Earth Sciences*, 67:89–99.
- 754 Salgado, A. A. R., Santos, L. J. C., and Paisani, J. C. (2019). *The physical geography of*
755 *Brazil*. Springer. Publication Title: Springer.
- 756 Salgado-Labouriau, M. L., Barberi, M., Ferraz-Vicentini, K. R., and Parizzi, M. G. (1998).
757 A dry climatic event during the late Quaternary of tropical Brazil. *Review of Palaeob-*
758 *otany and Palynology*, 99(2):115–129.
- 759 Silva, A. C., Horák-Terra, I., Barral, U. M., Costa, C. R., Gonçalves, S. T., Pinto, T.,
760 Christófaró Silva, B. P., Cunha Fernandes, J. S., Mendonça Filho, C. V., and Vidal-
761 Torrado, P. (2020). Altitude, vegetation, paleoclimate, and radiocarbon age of the basal
762 layer of peatlands of the Serra do Espinhaço Meridional, Brazil. *Journal of South Amer-*
763 *ican Earth Sciences*, 103(June):102728.
- 764 Skov, D. S., Egholm, D. L., Jansen, J. D., Sandiford, M., and Knudsen, M. F. (2019).
765 Detecting landscape transience with in situ cosmogenic ^{14}C and ^{10}Be . *Quaternary*
766 *Geochronology*, 54(June):101008.

- 767 Stone, J. O. (2000). Air pressure and cosmogenic isotope production. *Journal of Geophys-*
768 *ical Research: Solid Earth*, 105(B10):23753–23759. Publisher: American Geophysical
769 Union.
- 770 Struck, M., Jansen, J. D., Fujioka, T., Codilean, A. T., Fink, D., Egholm, D. L., Fülöp,
771 R.-H., Wilcken, K. M., and Kotevski, S. (2018). Soil production and transport on
772 postorogenic desert hillslopes quantified with ^{10}Be and ^{26}Al . *GSA Bulletin*, 130(5-
773 6):1017–1040.
- 774 von Blanckenburg, F. (2005). The control mechanisms of erosion and weathering at basin
775 scale from cosmogenic nuclides in river sediment. *Earth and Planetary Science Letters*,
776 237(3-4):462–479.
- 777 Wang, X., Auler, A. S., Edwards, R. L., Cheng, H., Ito, E., Wang, Y., Kong, X., and
778 Solheid, M. (2007). Millennial-scale precipitation changes in southern Brazil over the
779 past 90,000 years. *Geophysical Research Letters*, 34(23):L23701. Publisher: American
780 Geophysical Union.
- 781 West, N., Kirby, E., Bierman, P., and Clarke, B. A. (2014). Aspect-dependent variations
782 in regolith creep revealed by meteoric ^{10}Be . *Geology*, 42(6):507–510.
- 783 Willenbring, J. K. and Jerolmack, D. J. (2016). The null hypothesis: globally steady rates
784 of erosion, weathering fluxes and shelf sediment accumulation during Late Cenozoic
785 mountain uplift and glaciation. *Terra Nova*, 28(1):11–18.

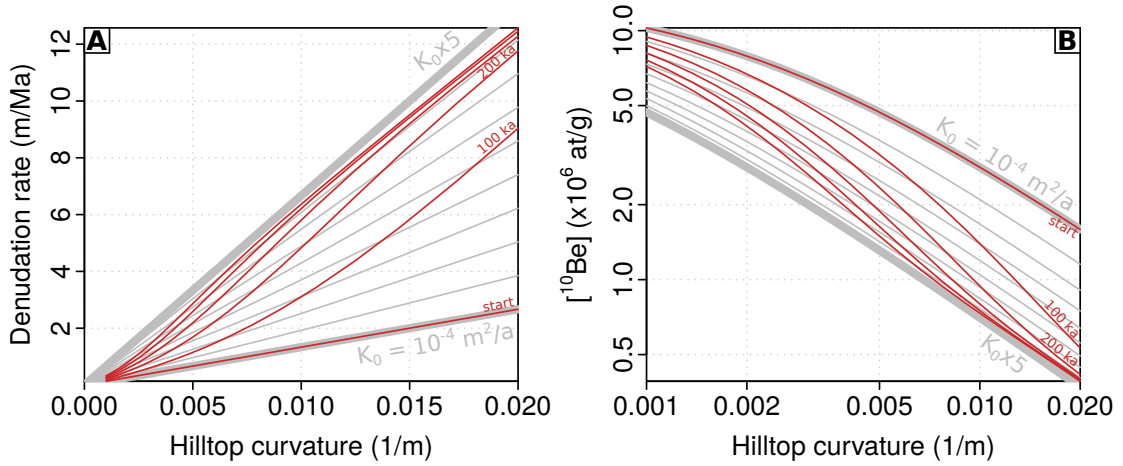


Figure 1: Illustration of the manifestation of transience in landscapes from the confrontation of cosmogenic nuclide data with high resolution topographic metrics. (A) Evolution of the relationship between hilltop curvature (C_{HT}) and ^{10}Be -derived denudation rate E , as a response to a 5-fold increase in sediment transport coefficient K . Thick grey lines are the starting and final steady-state situations. Thin grey lines are steady state relations for intermediate sediment transport coefficients (equation 5). Red curves display the transient evolution at 100 ka intervals. (B) Same as previous panel but for ^{10}Be concentration against C_{HT} (log axes). Note that we consider hillslope morphology, and thus hilltop curvature, to be stable over a time scale of a few 100s ka. This approximation is justified by the hillslope response time of the order of 1 Ma implied by the low sediment transport coefficient considered here.

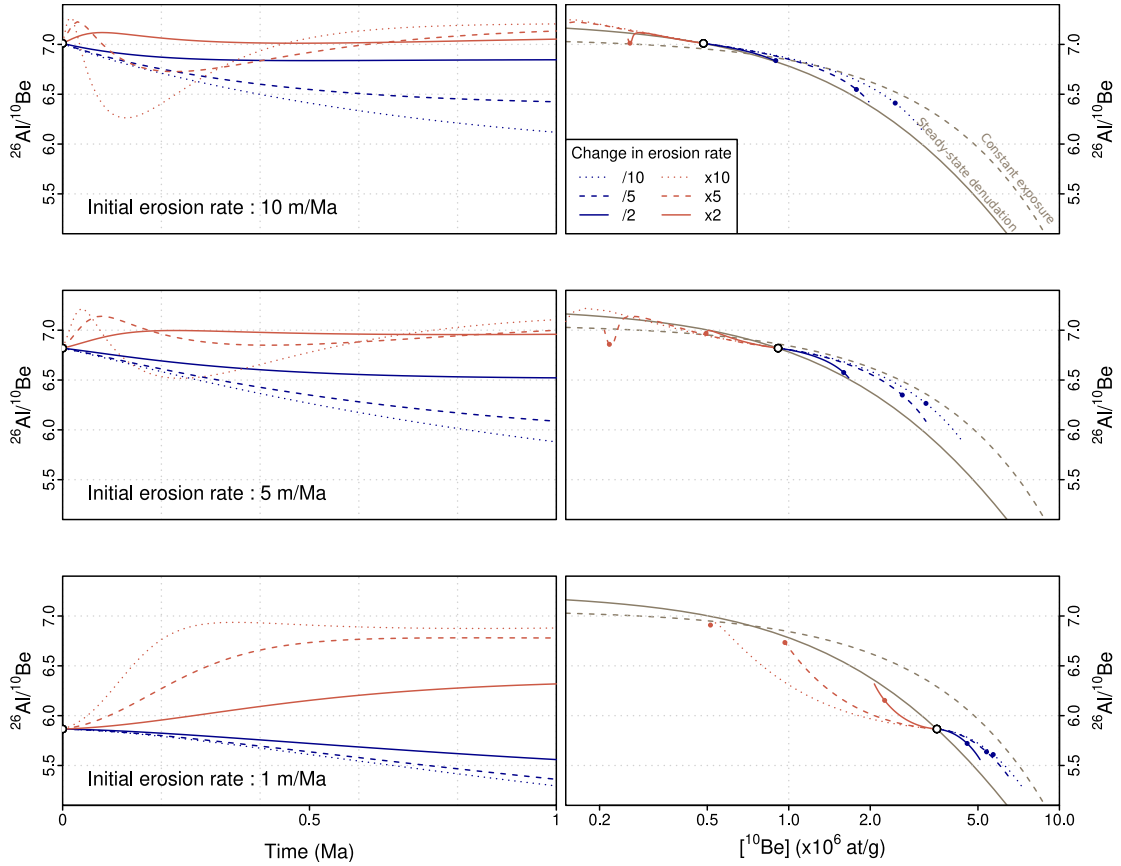


Figure 2: Responses of ^{10}Be and ^{26}Al surface concentrations and ratio to 2, 5 and 10-fold increases or decreases in denudation rates. Left panels display the evolution through time of the $^{26}\text{Al}/^{10}\text{Be}$ ratio, since the onset of the perturbation. Right panels display the corresponding evolution in a two-nuclides plot. White and colored circles indicate the starting points and 0.5 Ma mark, respectively. Solid and dashed brown curves correspond to expectations for steady-state erosion and a constantly exposed surfaces, respectively. Production rates are calculated for the average conditions at the sampled sites in the Serra do Cipó (Fig. 3), using a time-independent scaling scheme [Stone, 2000].

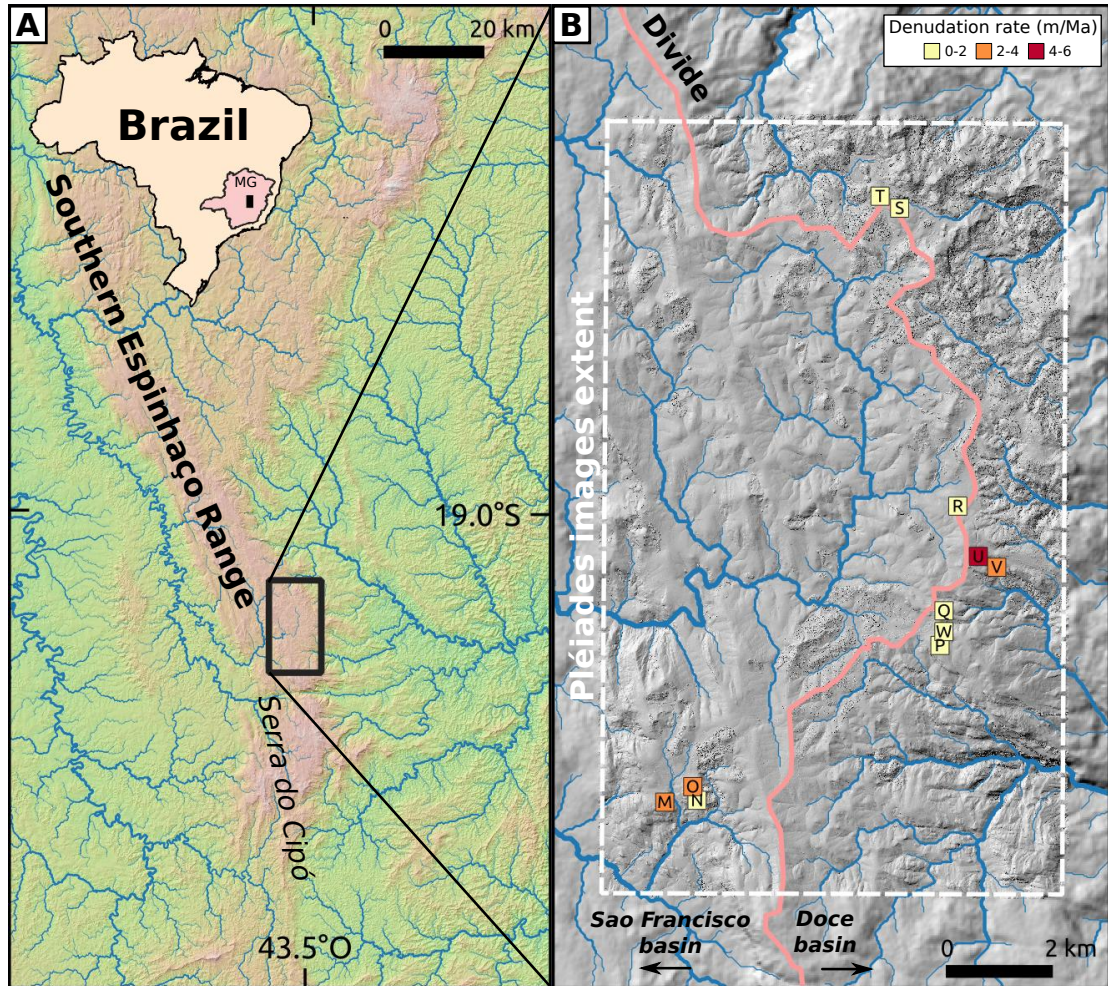


Figure 3: (A) Situation of the Southern Espinhaço Range in Minas Gerais State. (B) Location of sampled hilltop sites in the Serra do Cipó Range. Color scale indicates calculated steady-state denudation rates from ^{10}Be concentrations (m/Ma). Dashed rectangle is the extent of the Pléiades images triplet used to compute a high resolution Digital Surface Model (DSM). Pink line is the divide between the São Francisco and Doce river basins.

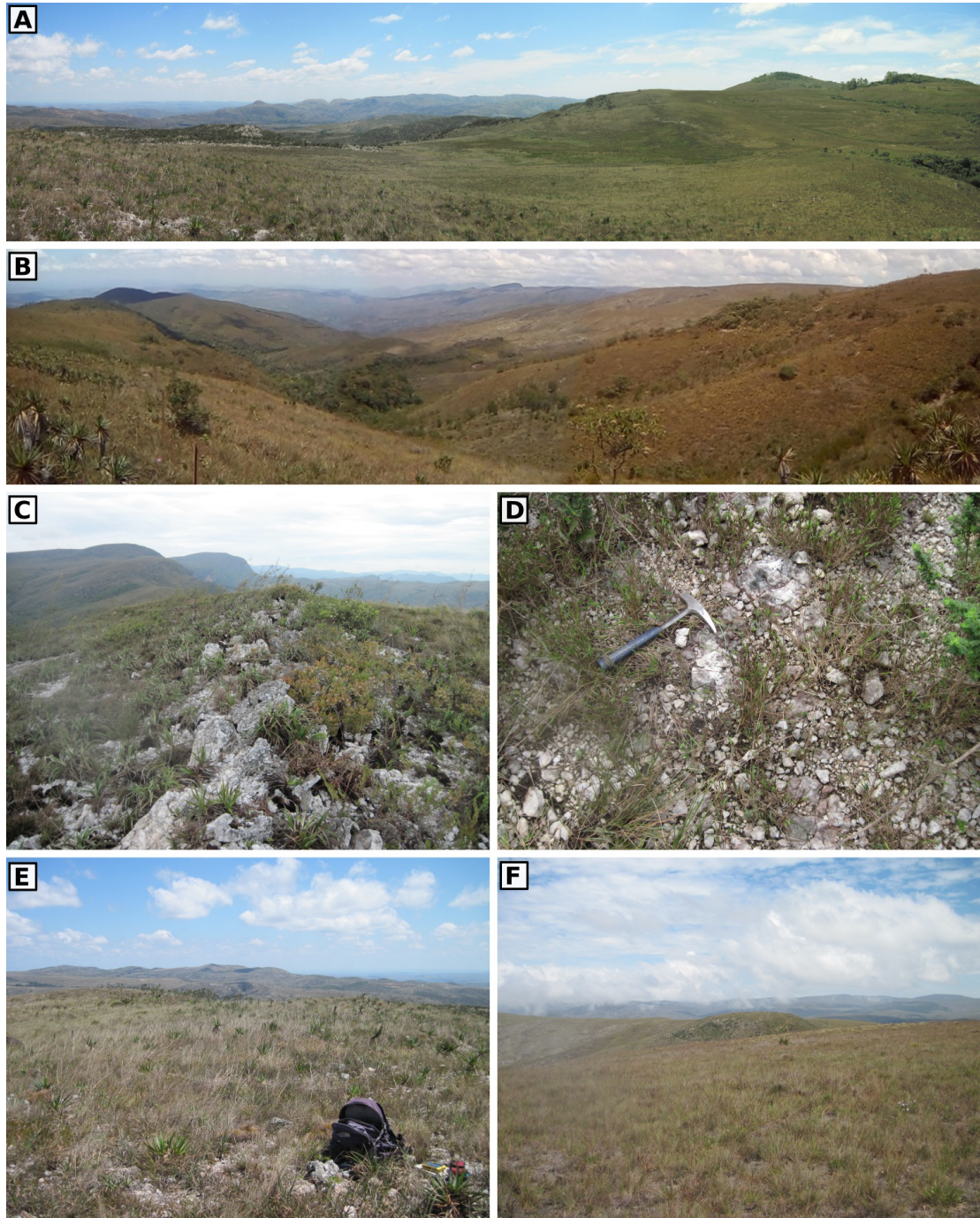


Figure 4: Sampling sites pictures. (A) View on Serra do Cipó landscape, toward the East from site M. (B) View on Serra do Cipó landscape, toward the East from site T. (C) Quartz vein at hilltop sampling site N. (D) Surface of hilltop sampling site W, with quartz vein embedded in the regolith and small quartz fragments. (E) Hilltop sampling site M. (F) View toward site W.

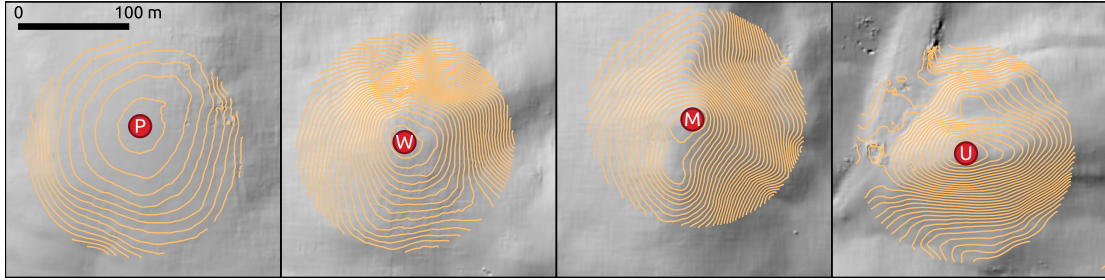


Figure 5: Shaded Pléiades Digital Surface Model (DSM) for 4 selected hilltop sites. Spacing of elevation contours is 1 m.

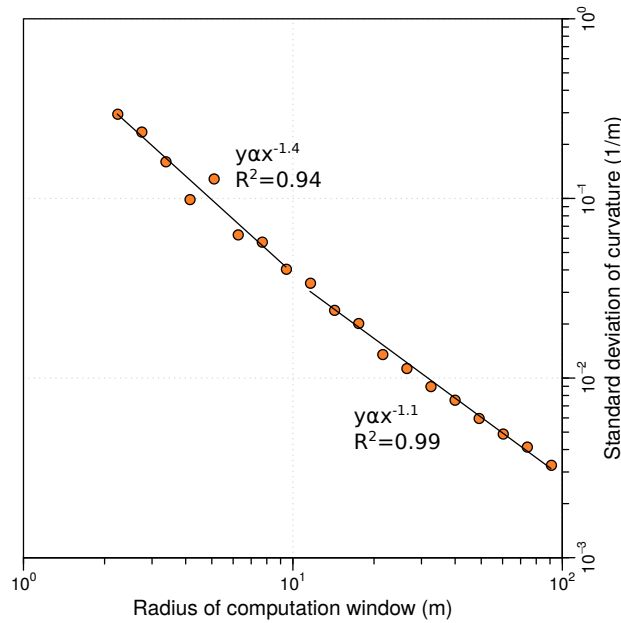


Figure 6: Evolution of the standard deviation of curvature as a function of the radius of the analysis window used to fit the quadratic surface of equation 7. 80×10^3 measurement points were sampled from the Pléiades DSM. A slight scaling break occurs at ~ 10 m radius for the analysis window and this size is used in the curvature computation. We note that the scaling break is less pronounced than in the results of [Roering et al. \[2010\]](#), due to the gentler variations in elevation of the Serra do Cipó hillslopes and the absence of trees, as opposed to the rugged and densely forested landscape of the Oregon Coast Range.

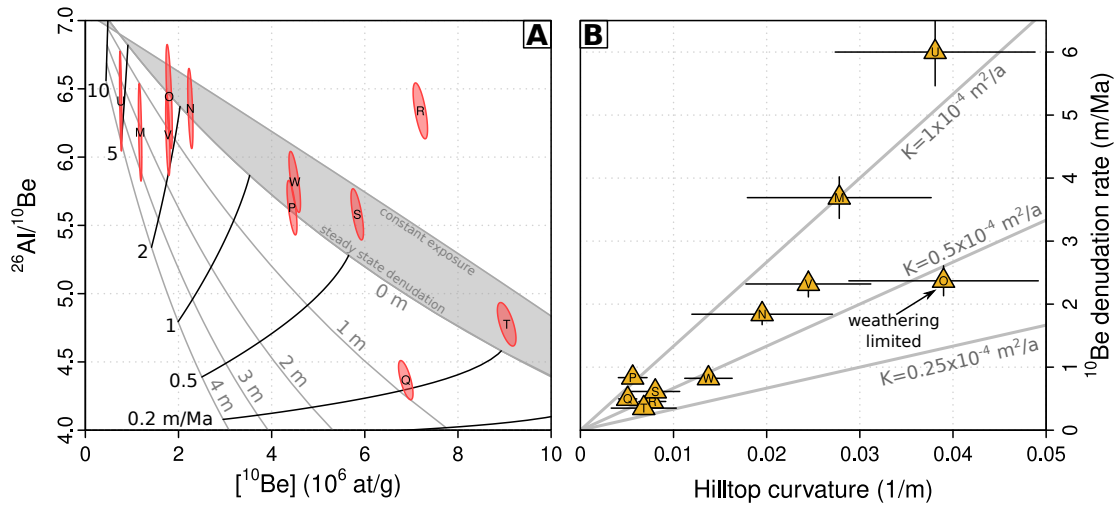


Figure 7: (A) Two-nuclides plot for the samples collected at hilltops (1σ confidence ellipses). See figure 3 for sites locations. Grey-filled area indicates the region between the steady-state surface denudation and constant exposure scenarios. Grey and black lines correspond to various regolith mixing-depth and denudation rates, respectively, according to the model of Foster et al. [2015]. Scaling according to Stone [2000]. (B) Denudation rate calculated from measured ^{10}Be concentrations as a function of hilltop curvature computed from the Pléiades DSM. Grey lines correspond to equation 5 with various values of the sediment transport coefficient.

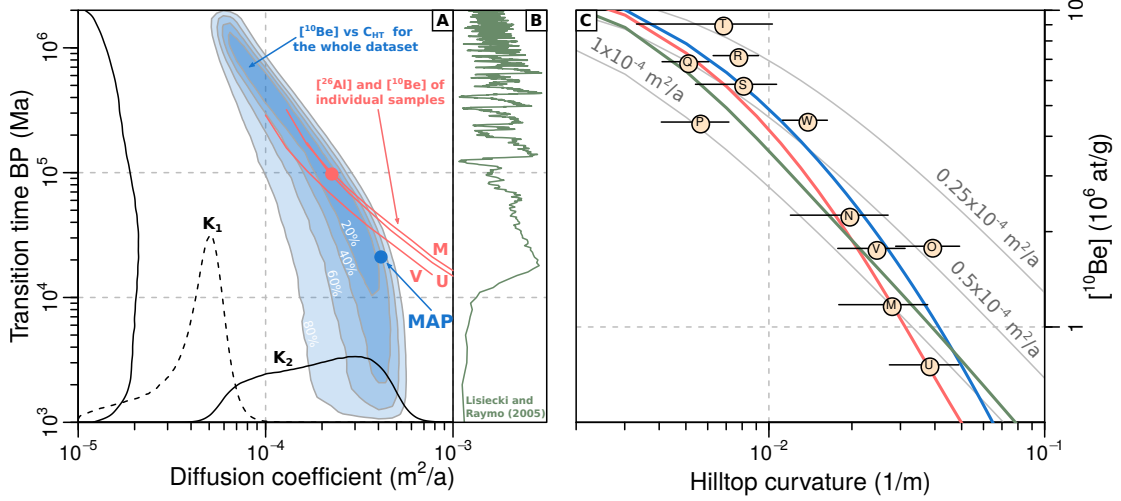


Figure 8: (A) Result of the MCMC inversion based on a 2-stages history set by 3 parameters: the initial (K_1) and final (K_2) sediment transport coefficients and the transition time T between the two. Blue shaded contours are highest posterior density region for T against K_2 , and the filled blue circle indicates the Maximum A posteriori Probability (MAP). Solid lines are marginal probability densities for K_2 and T , dashed line corresponds to K_1 . Red lines correspond to parameters combination allowing to predict the ^{10}Be and ^{26}Al concentrations within 1σ of the measured values (K_1 is set at $4 \times 10^{-5} m^2/a$). Red filled circle is a manually set parameters combination. (B) Marine $\delta^{18}O$ stack from Lisiecki and Raymo [2005] (log time scale). (C) Comparison of hilltop curvature (C_{HT}) and ^{10}Be concentrations. Grey lines are predictions for different time-constant sediment transport coefficients scenarios. Blue and red curves correspond to the predictions associated with sets of parameters from the filled circles on panel A. Dark green curve corresponds to the predictions with a sediment transport coefficient evolution mapped on the $\delta^{18}O$ curve, ranging from 10^{-5} to $3 \times 10^{-4} m^2/a$.

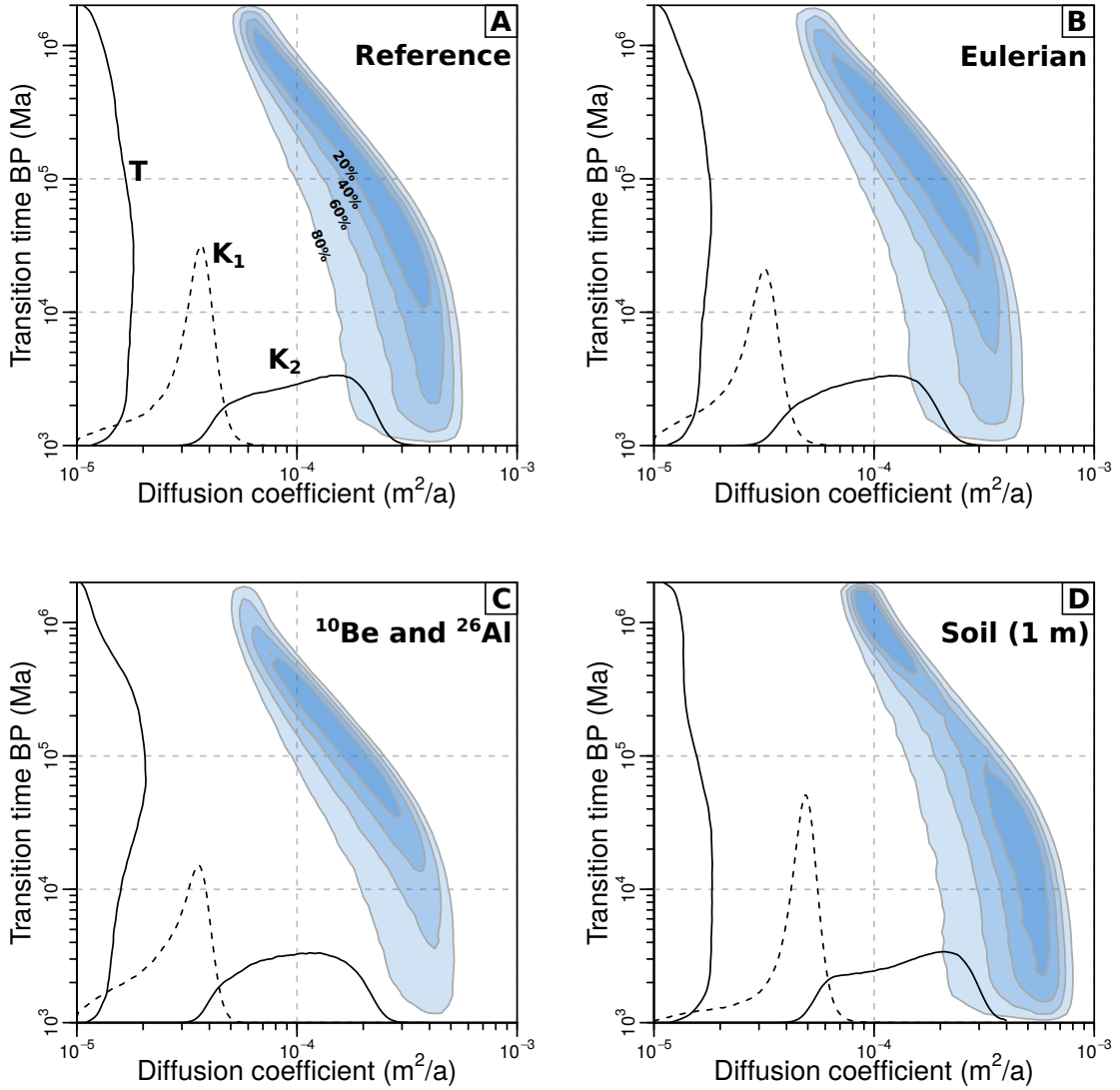


Figure 9: Tests of the influence of various aspects of the modelling approach on the inverted distributions for K_1 , K_2 and T . (A) Reference model (same as Fig. 8). Result of a MCMC inversion based on a 2-stages history set by 3 parameters: the initial (K_1) and final (K_2) sediment transport coefficients and the transition time T between the two. Blue shaded contours are highest posterior density region for T against K_2 . Solid lines are marginal probability density for K_2 and T , dashed line corresponds to K_1 . (B) Same as reference model but forward problem is solved with an Eulerian approach [Knudsen et al., 2019], using the time-independent Stone [2000] scaling and an exponential model for the muonic production at depth, with parameters from Braucher et al. [2011]. This simplified and computationally much faster Eulerian scheme provides essentially the same results as the reference model. (C) Same as reference model but using both ^{10}Be and ^{26}Al concentrations (only ^{10}Be data is used in the reference model). (D) Same as reference model, but the density decreases to 1.7 during the last 1 m of the exhumation history, to test the influence of density change associated with a regolith layer.

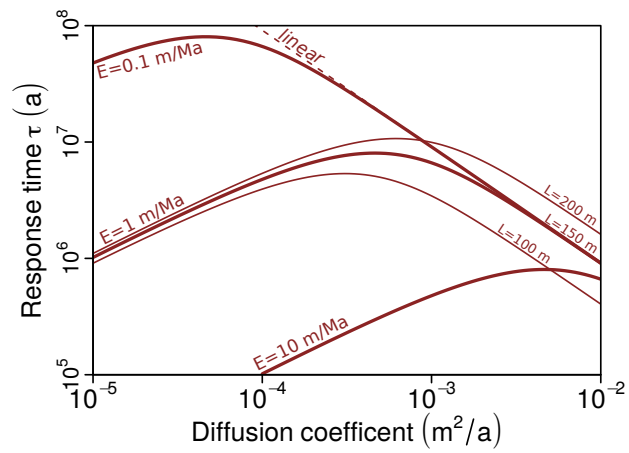


Figure 10: Adjustment time-scales of hillslopes based on linear (dashed lines) and non-linear (solid lines) evolution models [Roering et al., 2001; Hurst et al., 2012], for different values of the erosion rate E and hillslope length L .

Table 1: Cosmogenic nuclides data :¹⁰Be results

Mass ^e (g)	Be carrier ^b (g)	¹⁰ Be/ ⁹ Be ^{c,d,e,f} ($\times 10^{-12}$)	[¹⁰ Be] ^d ($\times 10^6$ at/g)	¹⁰ Be denudation rate ^{d,g,h} (m/Ma)	τ^i (Ma)	
M	16.22	0.1521	0.624 \pm 0.013	1.176 \pm 0.024	3.69 \pm 0.33 (3.46)	0.2
N	16.84	0.1531	1.23 \pm 0.02	2.254 \pm 0.037	1.84 \pm 0.17 (1.67)	0.3
O	9.8	0.153	0.573 \pm 0.014	1.798 \pm 0.045	2.37 \pm 0.24 (2.19)	0.3
P	20.87	0.1529	2.999 \pm 0.048	4.437 \pm 0.071	0.83 \pm 0.09 (0.68)	0.7
Q	21.85	0.1519	4.898 \pm 0.073	6.879 \pm 0.103	0.5 \pm 0.06 (0.33)	1.2
R	21.65	0.1527	5.048 \pm 0.072	7.192 \pm 0.103	0.46 \pm 0.06 (0.29)	1.3
S	21.17	0.1543	3.966 \pm 0.06	5.838 \pm 0.089	0.61 \pm 0.07 (0.45)	1.0
T	17.82	0.1533	5.205 \pm 0.076	9.046 \pm 0.132	0.35 \pm 0.05 (0.18)	1.7
U	20.11	0.1475	0.516 \pm 0.011	0.759 \pm 0.017	6 \pm 0.54 (5.7)	0.1
V	19.77	0.1525	1.139 \pm 0.02	1.77 \pm 0.031	2.32 \pm 0.21 (2.14)	0.3
W	20.02	0.1536	2.902 \pm 0.053	4.495 \pm 0.082	0.82 \pm 0.09 (0.67)	0.7

^a Dissolved pure quartz mass.

^b Be in-house carrier mass, ~ 150 μ l at 3.025 $\times 10^{-3}$ g/g [Merchel et al., 2008].

^c ¹⁰Be/⁹Be ratios were calibrated against the STD-11 standard by using an assigned value of $1.191 \pm 0.013 \times 10^{-11}$ [Braucher et al., 2015].

^d Uncertainties are reported at the 1σ level.

^e Uncertainties on isotopic ratios are calculated according to the standard error propagation method using the quadratic sum of the relative errors and include a conservative 0.5% external machine uncertainty [Arnold et al., 2010], the uncertainty on the certified standard ratio, a 1σ uncertainty associated to the mean of the standard ratio measurements during the measurement cycles, a 1σ statistical error on counted events and the uncertainty associated with the chemical and analytical blank corrections.

^f One process blank was treated and measured with our samples, yielding a ¹⁰Be/⁹Be ratio of $3.53 \pm 0.34 \times 10^{-15}$. It corresponds to an upper 1σ bound of 120×10^3 ¹⁰Be atoms for the background level in this blank, which is at least 120 times lower than the number of ¹⁰Be atoms in the dissolved sample masses (600 times lower in average over our dataset).

^g Denudation rates were calculated with the online calculator described in Balco et al. [2008] and the nuclide specific LSD scaling scheme [Lifton et al., 2014], using the CRONUS-Earth calibration dataset [Borchers et al., 2016] for the calculation of spallation production rates and muon production rates according to Balco [2017]. We use 160 g/cm² for the effective neutron attenuation length in rock, and a density of 2.65 g/cm³. No shielding correction was considered for the hilltop sites we sampled.

^h Numbers in parenthesis are the denudation rates computed with Lal/Stone time-independent scaling.

ⁱ Integration time scales for ¹⁰Be denudation rates [von Blanckenburg, 2005].

Table 2: Cosmogenic nuclides data : ^{26}Al results and comparison with ^{10}Be results from table 1

Sample	[Al] natural ^a (ppm)	Al carrier ^b (g)	$^{26}\text{Al}/^{27}\text{Al}^{c,d,e}$ ($\times 10^{-12}$)	$[^{26}\text{Al}]^d$ ($\times 10^6$ at/g)	^{26}Al denudation rate ^f (mm/ka)	τ^g (Ma)	$^{10}\text{Be}/^{26}\text{Al}$
M	17.8	1.2448	3.749 ± 0.12	7.27 ± 0.236	3.76 ± 0.54	0.2	6.18 ± 0.24
N	16.1	1.2227	7.834 ± 0.199	14.327 ± 0.369	1.67 ± 0.26	0.4	6.36 ± 0.19
O	114.3	0.6983	3.534 ± 0.105	11.589 ± 0.352	2.2 ± 0.34	0.3	6.44 ± 0.25
P	17.3	1.2211	16.83 ± 0.282	24.976 ± 0.43	0.79 ± 0.15	0.8	5.63 ± 0.13
Q	23.2	1.2278	20.568 ± 0.316	30.037 ± 0.475	0.62 ± 0.13	1.0	4.37 ± 0.1
R	60.4	1.0101	31.101 ± 0.484	45.586 ± 0.727	0.32 ± 0.1	1.9	6.34 ± 0.14
S	20.9	1.2229	21.864 ± 0.346	32.577 ± 0.53	0.56 ± 0.12	1.1	5.58 ± 0.12
T	20.7	1.2355	24.249 ± 0.391	43.197 ± 0.716	0.37 ± 0.1	1.6	4.78 ± 0.11
U	17.9	1.1851	3.256 ± 0.098	4.867 ± 0.149	6.05 ± 0.81	0.1	6.41 ± 0.24
V	16.9	1.0800	7.835 ± 0.208	10.91 ± 0.294	2.27 ± 0.34	0.3	6.16 ± 0.2
W	22.0	1.1442	17.57 ± 0.303	26.155 ± 0.462	0.74 ± 0.14	0.8	5.82 ± 0.15

^a Naturally occurring Al measured by ICP-OES. Note the high concentration for sample O, which is the only one from the quartzite bedrock instead of the quartz veins.

^b Al Carrier mass, 993 ± 4 ppm concentration.

^c The measured $^{26}\text{Al}/^{27}\text{Al}$ ratios were normalized to the in-house standard SM-Al-11 whose ratio of $7.401 \pm 0.064 \times 10^{-12}$ [Arnold et al., 2010] has been cross-calibrated against primary standards from a round-robin exercise [Merchel and Bremser, 2004].

^d Uncertainties are reported at the 1σ level.

^e A process blank yielded a ratio of $2.01 \pm 0.45 \times 10^{-14}$. It corresponds to an upper 1σ bound of 730×10^3 ^{26}Al atoms for the background level in this blank, which is at least 130 times lower than the number of ^{26}Al atoms in the dissolved sample masses (610 times lower in average over our dataset)

^f Procedures for the calculation of denudation rates are identical to the ones described in table 1.

^g Integration time scales for ^{26}Al denudation rates [von Blanckenburg, 2005].

Table 3: Site locations and hilltop curvature measurements

Site	Latitude ($^{\circ}$)	Longitude ($^{\circ}$)	Altitude (m)	Hilltop curvature (m^{-1})
M	-19.2637	-43.5558	1313	0.028 ± 0.010
N	-19.2614	-43.5508	1354	0.020 ± 0.008
O	-19.2612	-43.5508	1353	0.039 ± 0.010
P	-19.2361	-43.5058	1355	0.006 ± 0.002
Q	-19.2301	-43.5051	1365	0.005 ± 0.001
R	-19.2119	-43.5027	1335	0.008 ± 0.001
S	-19.1594	-43.5156	1380	0.008 ± 0.003
T	-19.1582	-43.5174	1379	0.007 ± 0.003
U	-19.2206	-43.4989	1337	0.038 ± 0.011
V	-19.2218	-43.4968	1301	0.024 ± 0.007
W	-19.2337	-43.5050	1357	0.014 ± 0.003